

The Nulling Interferometry Cryogenic Experiment (NICE): Architecture, requirements, and preliminary warm precursor results

Thomas Birbacher^{a*}[†][□], Jonah T. Hansen^{a†}[□], Felix A. Dannert^a[□], Germain Garreau^a[□], Adrian M. Glauser^a[□], Ryan Meierhofer^a, Julio Pino Jiménez^a, Mohanakrishna Ranganathan^a[□], Sascha P. Quanz^{a,b}[□]

^aETH Zürich, Institute for Particle Physics & Astrophysics, Wolfgang-Pauli-Str. 27, 8093 Zurich, Switzerland

^bETH Zürich, Department of Earth and Planetary Sciences, Sonneggstrasse 5, 8092 Zurich, Switzerland

Abstract. The success of the Large Interferometer For Exoplanets (LIFE) space mission depends on measuring the faint mid-infrared emission spectra of exoplanets while suppressing the glare of a host star. This requires an instrument capable of high-contrast nulling interferometry with exceptional sensitivity. While previous testbeds have proven the principle of deep, stable nulls, they have not combined high contrast with the high throughput and cryogenic operation required for LIFE. Here, we present the architecture of the Nulling Interferometry Cryogenic Experiment (NICE), a mid-infrared nulling testbed, to increase the technological readiness of LIFE. We derive the laboratory requirements necessary to validate the LIFE beam combiner and present the optical design of NICE. Finally, we report results from the ambient “Warm Bench” precursor, which has successfully demonstrated the required null depth ($< 10^{-5}$) using a polarized narrowband $4.7\text{ }\mu\text{m}$ source, and the required throughput ($> 17\%$) using one of the two nulling channels.

Keywords: Nulling interferometry, NICE, LIFE, mid-infrared, cryogenics, exoplanets.

*Send correspondence to Thomas Birbacher, thomabir@phys.ethz.ch.

† Joint first authors for this article.

1 Introduction

The Large Interferometer For Exoplanets¹ (LIFE) space mission is currently the most promising mission concept for systematically characterizing the atmospheres of terrestrial exoplanets in the mid-infrared. LIFE aims to measure the emission spectra of ≈ 50 temperate terrestrial exoplanets in the habitable zones of nearby solar-type stars, and thus quantify the presence of a large set of spectral biosignatures.²

To overcome the contrast between planet and star, LIFE is designed as a nulling interferometer, a concept originally proposed by Bracewell³ for exoplanet detection. In its simplest form, it consists of two telescope apertures that combine their light such that the on-axis star is nulled out through destructive interference, while the off-axis planet undergoes constructive interference. The reference design⁴ for LIFE is a Double-Bracewell nullder,⁵ with four formation-flying collector telescopes and a central combiner spacecraft.

Because of the faintness of temperate terrestrial exoplanets ($\approx 1\text{ ph/s/m}^2/\mu\text{m}$ at $10\text{ }\mu\text{m}$ for an Earth-twin at 10 pc),⁶ and the targeted wavelength range in the mid-infrared ($4\text{ }\mu\text{m}$ to $18.5\text{ }\mu\text{m}$), LIFE depends on a space-based, cryogenic, high-throughput instrument to achieve the required sensitivity. To reach a null deep enough for the characterization of such a planet ($\approx 10^{-5}$ raw null depth before post-processing), optical path-length differences in the instrument have to be

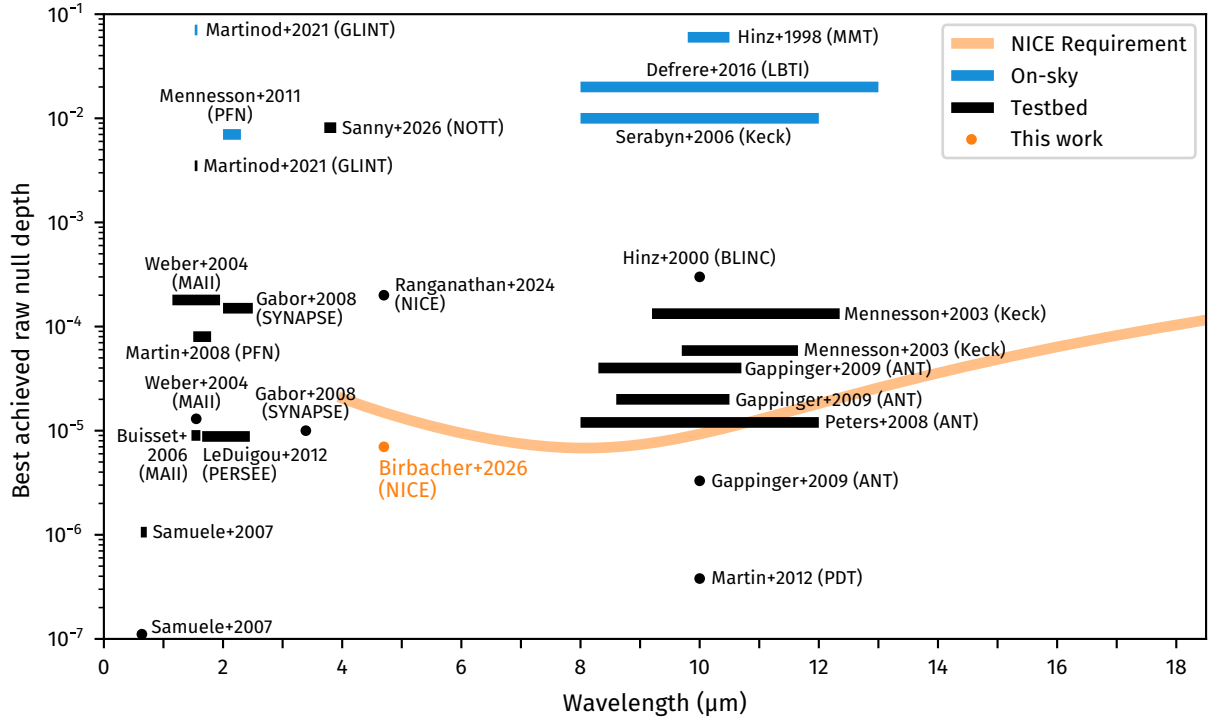


Fig 1: A sample of the best measured raw null depths with on-sky nulling facilities and testbeds, compared with the requirement for NICE, derived in Section 2. Rectangular markers denote nulls with more than 2 % spectral bandwidth, and circles denote narrowband nulls.

controlled to the nanometer-level, and intensity and polarization mismatches reduced to the sub-percent level. Combined, these factors necessitate an exceptionally stable optical setup with high demands on throughput and alignment accuracy, housed in a low-vibration cryostat.

Attempts towards such an instrument have been made before, notably for ESA’s Darwin^{7,8} and NASA’s TPF-I^{9,10} missions. From ESA’s side, the SYNAPSE,¹¹ MAII,^{12,13} and PERSEE¹⁴ testbeds have measured stable nulls deeper than 10^{-5} from 1.1 μm to 3.4 μm . JPL’s Planet Detection Testbed¹⁵ (PDT) has achieved $< 10^{-6}$ nulls at 10 μm in combination with a detection of a simulated planet, and the Achromatic Nulling Testbed^{16,17} (ANT) has demonstrated a 10^{-5} null covering a broad spectral band from 8 μm to 12 μm . In addition to these testbeds, several astronomical nullers have shown on-sky null depths from roughly 10^{-3} to 10^{-1} , from the near- to the mid-infrared. These include the Multiple-Mirror Telescope (MMT) Nuller,¹⁸ the Keck Interferometer Nuller,^{19,20} the Palomar Fiber Nuller^{10,21} (PFN), the Large Binocular Telescope Interferometer (LBTI) nuller,^{22,23} GLINT,²⁴⁻²⁶ and the upcoming Asgard/NOTT.²⁷⁻²⁹ A sample of the best nulls achieved on-sky and by testbeds so far is summarized in Fig. 1.

Despite tremendous progress in the field, no hardware has yet combined stable 10^{-5} nulls with a broadband cryogenic instrument. The specific high-sensitivity, high-contrast range relevant for LIFE remains experimentally unexplored, and nulling across the full two-octave science bandwidth has never been demonstrated. Before the space mission can be realized, a ground-based laboratory testbed is thus needed to develop the required technologies and demonstrate the measurement in a realistic environment.

We are building the Nulling Interferometry Cryogenic Experiment³⁰ (NICE) laboratory testbed

to fill this technological gap. NICE will be designed as the first cryogenic nullder focused on high sensitivity and full coverage of the LIFE spectral band, while still achieving the deep and stable nulls that have been demonstrated on previous projects. NICE will start as a Single-Bracewell nullder,³ collecting light from a simulated star with two apertures, to test the capability to reach deep raw nulls and thus suppress photon noise from the star. Later, it may be extended to a Double-Bracewell design with four beams, representative of the full LIFE beam combiner where a final cross-combiner stage further increases the achievable contrast.

In this paper, we define the laboratory requirements necessary to validate the LIFE beam combiner (Section 2), and present the conceptual layout of NICE to meet these requirements (Section 3). To prototype the cryogenic instrument, we are building the NICE “Warm Bench”, an ambient precursor that has already achieved the required null depth with a narrowband 4.7 μm laser (Section 4.1), as well as the required throughput (Section 4.2). We discuss our results in Section 5, provide an outlook of future work in Section 6, and conclude in Section 7.

2 Requirements

NICE is a technology demonstrator for the LIFE mission, and the requirements for NICE must be derived such that it could operate as the nulling beam combiner in LIFE. At the top level, NICE is similar to other high-contrast imaging systems, largely characterized by two key performance metrics: sensitivity and contrast.³¹ Specifically, NICE should be able to receive two input beams and combine them such that light from a simulated on-axis star is nulled out, while light from a simulated off-axis planet is transmitted to the detector with high efficiency.

Efforts are still ongoing to finalize the LIFE requirements, such that they can systematically be traced back to the LIFE science goals. A tentative set of requirements on the LIFE measurement performance has already been derived,³² and we choose this as a starting point for deriving the NICE requirements. The requirements we set for NICE, summarized in Table 1, are intentionally more ambitious than necessary to account for potential upcoming changes in the LIFE requirements.

2.1 Raw null depth

The primary purpose of the nullder is to suppress light from a star through destructive interference, and thus reduce the photon noise it contributes to the measurement. This capability is qualified by the raw null depth, the intensity ratio of the destructive (I_-) to constructive interference (I_+), which for a two-beam nullder is defined as

$$N = \frac{I_-}{I_+} = \frac{I_-}{I_1 + I_2 + 2\sqrt{I_1 I_2}}, \quad (1)$$

where I_1 and I_2 are the intensities of the single beams without interference, measured on the science detector at the destructive output. We put a requirement on the raw null depth because it is easily measurable, while factors that contribute to the null depth, such as differential optical path length and polarization mismatches, are harder to measure. In practice, there will be two factors that limit the null depth achievable with an on-sky instrument: fundamental astrophysical noise and perturbations by the instrument.

First, fundamental astrophysical noise terms, studied previously in the context of LIFE,^{6,33} will leak through even in an ideal nullder. For example, consider that while an on-axis point source

Table 1: Requirements for NICE to demonstrate the feasibility of the LIFE nulling beam combiner.

<i>During entire observation (with regular re-calibration):</i>	
Mean raw null depth	$2 \cdot 10^{-5}$ at 4 μm , $7 \cdot 10^{-6}$ at 8 μm , $9 \cdot 10^{-6}$ at 10 μm $1 \cdot 10^{-4}$ at 18 μm
Wavelength range	9 μm to 11 μm (requirement) 4 μm to 5 μm (requirement) 4 μm to 18.5 μm (goal)
Photon conversion efficiency (planet)	20 %
Throughput	34 %
Detector quantum efficiency	60 %
Stability without re-calibration	100 s at least
Calibration time	10 s (goal)
Cryostat temperature	12 K to 15 K
<i>At planet modulation timescales (band-pass from 170 μHz to 330 μHz):</i>	
Raw null depth RMS	$3 \cdot 10^{-7}$ at 8 μm
Optical path-length difference RMS	0.3 nm
Intensity RMS (each beam)	0.02 %

would be perfectly nulled, an extended source, such as a star, will be partially transmitted. This effect is called stellar geometric leakage³⁴ and dominates the noise budget at shorter wavelengths. At longer wavelengths, the limit is set by the thermal background, such as emission from the local-zodiacal and exozodiacal dust clouds. Importantly, while some of these background sources can be subtracted in post-processing, even for an ideal nulling interferometer they contribute photon noise, which degrades the planet signal-to-noise ratio (SNR).

Second, a real instrument is additionally subjected to phase and amplitude perturbations, such as residual noise from formation flying or vibrations. These perturbations, collectively called instrumental errors, deteriorate the quality of the null, which we model as a decrease of interferometric visibility, shown schematically in Fig. 2. We model the on-sky transmission T of the ideal instrument⁶ as

$$T(\theta) = \sin^2 \left(\frac{2\pi L \theta}{\lambda} \right),$$

where θ is the on-sky angle, L is the nulling baseline length, and λ is the observing wavelength. We model the perturbed transmission as a visibility degradation, $T'(\theta) = T(\theta)V + (1 - V)/2$, where V is the visibility. This allows us to translate between the on-axis null depth as would be measured by NICE, and the null depth over the full field of view as would be measured by LIFE.

To set a requirement on the raw null depth in NICE, we first consider an unperturbed instrument, observing an Earth-twin around a Solar analog, limited only by fundamental astrophysical photon noise sources. We then find the SNR that this ideal instrument can achieve as a function of wavelength, and demand that perturbations and errors in the beam combiner degrade this ideal SNR by no more than 10 %. A similar method was used in Appendix A of Dannert 2022.⁶ This argument is independent of parameters such as integration time and mirror diameter. The number of 10 % was chosen because it represents a reasonable trade-off between demands on the instrument and achievable SNR: beyond this number, we enter a regime of strongly diminishing

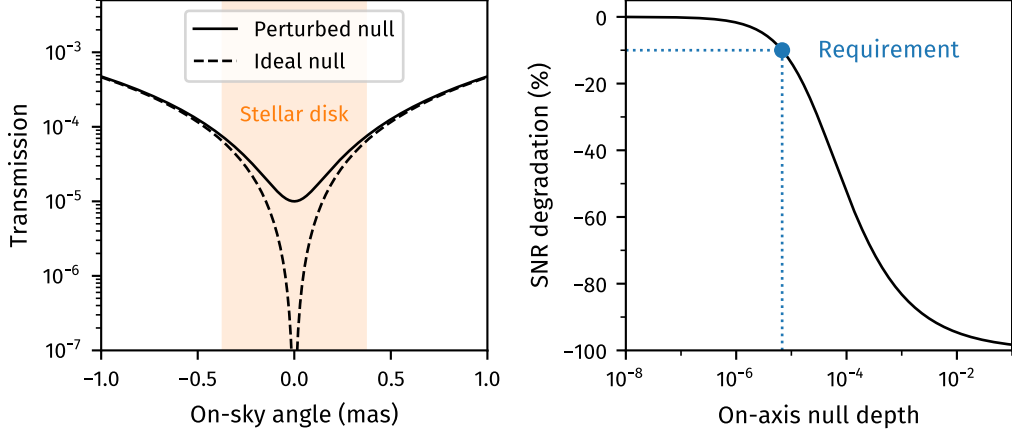


Fig 2: *Left:* Transmission of a Single-Bracewell nullder at $8\text{ }\mu\text{m}$ as a function of on-sky angle for an ideal instrument and a perturbed instrument with degraded visibility. The baseline is optimized for an Earth-twin around a Solar-type star (shaded region) at a distance of 10 pc. The transmission at an on-sky angle of zero is called the on-axis null depth. *Right:* The SNR of the instrument degrades as the on-axis null depth worsens because of increased stellar leakage, shown here at $8\text{ }\mu\text{m}$ wavelength. We set a requirement of at most 10 % reduction in SNR from instrument errors.

returns, as visible in Fig. 2. While this is a heuristic requirement, it ensures that fundamental noise sources dominate any contribution from the beam combiner.

The resulting requirement on the null depth in NICE is shown in Table 1. It reaches its deepest value of $7 \cdot 10^{-6}$ at $8\text{ }\mu\text{m}$, before relaxing by an order of magnitude towards the longer wavelengths. Improving the null depth beyond this requirement is of limited use, since fundamental astrophysical noise already strongly dominates in this regime.

2.2 Sensitivity

The scientific yield of the LIFE mission depends critically on the capability to collect planet photons with low loss. We define the photon conversion efficiency (PCE) of LIFE as the number of planet photons detected on the science detector, divided by the number of planet photons entering the primary apertures. Our reference design^{4,32} currently assumes four collectors with 3 m to 4 m mirrors, a characterization campaign of five years, a 1:5 ratio between calibration time and science time, and a PCE of 3.5 %. The reference PCE will likely increase in the future, but is expected to stay in a range between 3.5 % to 10 %, depending on the targeted optical design and assumptions on the exoplanet population.

To set a PCE requirement on NICE, we must account for the systems that are represented in NICE, and the systems that are not represented in NICE, such as the primary mirror, the beam transport to the beam combiner, a first stage of correction optics, and the cross-combiner that is used inside a four-beam Double-Bracewell instrument. Since we can test and characterize NICE in the lab, while the remaining system has not been experimentally verified, we chose to put a conservative 20 % PCE requirement on NICE, stricter than what would be justified by a simple throughput budget. Optimizing sensitivity even beyond this requirement is an ambition strongly worth pursuing, as gains in throughput can relax other parameters and reduce mission cost.³⁵

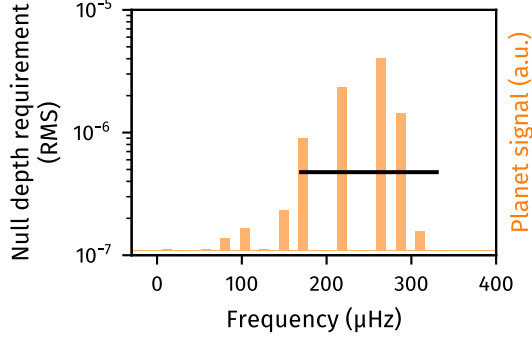


Fig 3: Requirement on the null depth power spectrum at 8 μm . Assuming one rotation of the array per day, NICE requires a stability of the null depth of $6 \cdot 10^{-7}$ RMS from 170 μHz to 330 μHz (black line) for a Single-Bracewell interferometer to act as the beam combiner in LIFE. The expected spectral signature of a planet is also shown.

We further break the PCE requirement down into a requirement on the throughput of the optics (34 %) and a requirement on the quantum efficiency (QE) of the detector (60 %).

2.3 Null stability

Slow drifts of the instrument lead to a measurement that could be mistaken for a planet signal, similar to how speckles can be mistaken for companions in single-aperture high-contrast imaging, and thus a requirement on the stability of the null depth is critical to achieve a confident measurement.³⁶ More specifically, LIFE records time-series of spectra, and the spatial resolution of LIFE — i.e. the capability to locate a planet and to distinguish two planets in the same system — is achieved through a rotation of the interferometric baselines over time. In the Fourier transform of this time series, we know that planet signals can only occur at specific harmonics of the rotation period of the array, as shown in Fig. 3. As a consequence, any noise in the null depth within this frequency range could be mistaken for a planet signal, and result in a false positive detection. It has been derived³² that a noise level of 0.6 nm RMS in OPD and 0.04 % RMS in beam intensity within 170 μHz to 330 μHz (assuming one baseline rotation per day) can be allowed for LIFE to achieve its science goals. This corresponds to a null depth RMS of $6 \cdot 10^{-7}$ RMS at 8 μm at these frequencies. To account for noise sources not modeled in NICE, such as formation flight and beam transfer to the combiner, we impose the stricter requirements in Table 1 on the testbed, corresponding to a $3 \cdot 10^{-7}$ null depth RMS.

2.4 Duty cycle and automatic recalibration

To meet the constraints on mean null depth and null depth stability, we expect regular calibrations during science observations. With the assumed 5:1 ratio between science observations and calibration for LIFE, we set the requirement that at most 10 % of operation time may be used for calibration procedures in NICE, accounting for NICE calibrating approximately half the number of beams as LIFE.

Previous benches, such as PERSEE³⁷ and the Planet Detection Testbed,¹⁵ used a dithering technique to find the reference point of the OPD and tip/tilt of the fiber injection: measuring either side of the current position and using prior information on the null to find the new reference point.³⁸ To properly constrain the phase and amplitude of both beams, ten measurements must

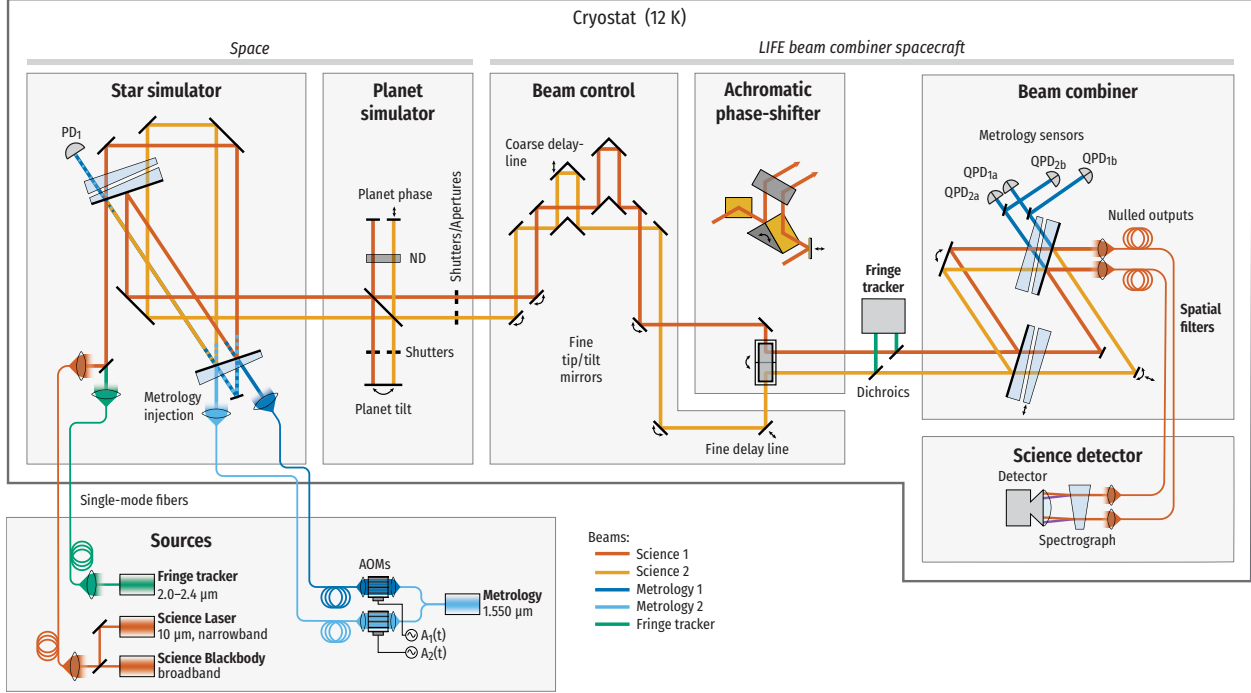


Fig 4: Preliminary optical diagram of NICE. QPDs are quadrant photodiodes for the metrology, and PDs are regular photodiodes. The electrical signals A_1 and A_2 are amplitude-modulated drive signals for the acousto-optic modulators (AOMs)

be made: eight for the pointing and shear (or lateral position) of each beam, and two for the OPD. From Appendix A of Hansen et al. (2023),³⁹ in order to be dominated by emission from zodiacal dust across the LIFE bandpass, one needs to integrate the dither on the order of 0.5 s to 1 s. Including settling time of the various piezo stages, this results in a calibration on the order of 10 s. Thus, the NICE measurement must be stable for at least 100 s to meet the requirement on duty cycle, and we target a calibration time of 10 s with realistic stellar flux levels.

3 Methods

The primary goal of NICE is to demonstrate the nulling beam combiner which lies at the heart of the LIFE beam combiner spacecraft. The optical system of NICE thus has to be representative of the space hardware, which demands a broadband, cryogenic, high-throughput instrument.

3.1 Optical setup

We show two optical diagrams in this section: the preliminary optical diagram of the cryogenic NICE bench (Fig. 4), and the optical diagram of the NICE Warm Bench (Fig. 5, Fig. 6) in its current state, which is the precursor experiment at ambient conditions, used for all measurements that follow. We focus our description on the cryogenic setup, and note the differences with the warm setup wherever they occur. To reduce differential chromatic and polarization errors in the science beams, we designed the setup such that it is symmetric, i.e. the two science beams undergo the same number of transmissions and reflections.

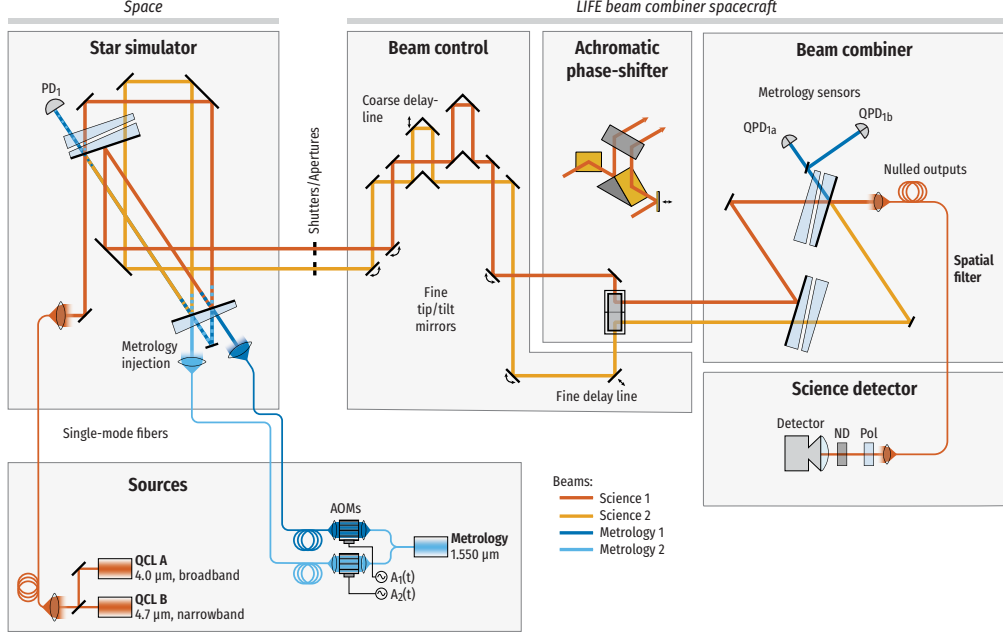


Fig 5: Optical diagram of the Warm Bench, a precursor for NICE at ambient conditions, as it was used for the measurements.

3.1.1 Sources

Since this is a laboratory testbed, we have to simulate the star. We aim to eventually cover the full LIFE science band of $4\text{ }\mu\text{m}$ to $18.5\text{ }\mu\text{m}$, which will likely be implemented as a broadband thermal blackbody. Multiple narrowband sources will be used for prototyping and characterization, as a blackbody source will not produce enough power for easy measurements. In addition to the science sources, we foresee separate sources for a fringe tracker and a laser metrology system, explained in more detail in Section 3.3.

On the Warm Bench, we chose to start with the short end of the science band, where requirements on geometric stability are most stringent and the thermal background of the lab is lower. We currently use two quantum-cascade lasers (QCLs) to simulate a star for the setup: One is a $4.0\text{ }\mu\text{m}$, 100 mW off-the-shelf laser with coherence length on the order of $\approx 100\text{ }\mu\text{m}$, and is used to find the central dark fringe, but not for nulling measurements, as it is a pulsed source. (This source has been recently replaced with a continuous-wave source for future broadband nulling experiments.) The other source is a $4.7\text{ }\mu\text{m}$, 100 mW continuous-wave laser with coherence length $> 10\text{ cm}$, developed in-house, and used as a narrowband source for nulling. The sources are located on a separate table, and are fed into the star simulator with single-mode fibers. Both lasers can be injected into the setup simultaneously, using a beam-splitter to couple into the same fiber. While we expect top-hat shaped beams from the LIFE collectors, all sources in the current setup have a Gaussian profile.

3.1.2 Star simulator

The single beam from a laser is split into two, representing beams received from two of the collector spacecraft. Because of its inherent symmetry, we use a modified Sagnac interferometer to simulate the star, where each beam undergoes an equal number of transmissions and reflections,

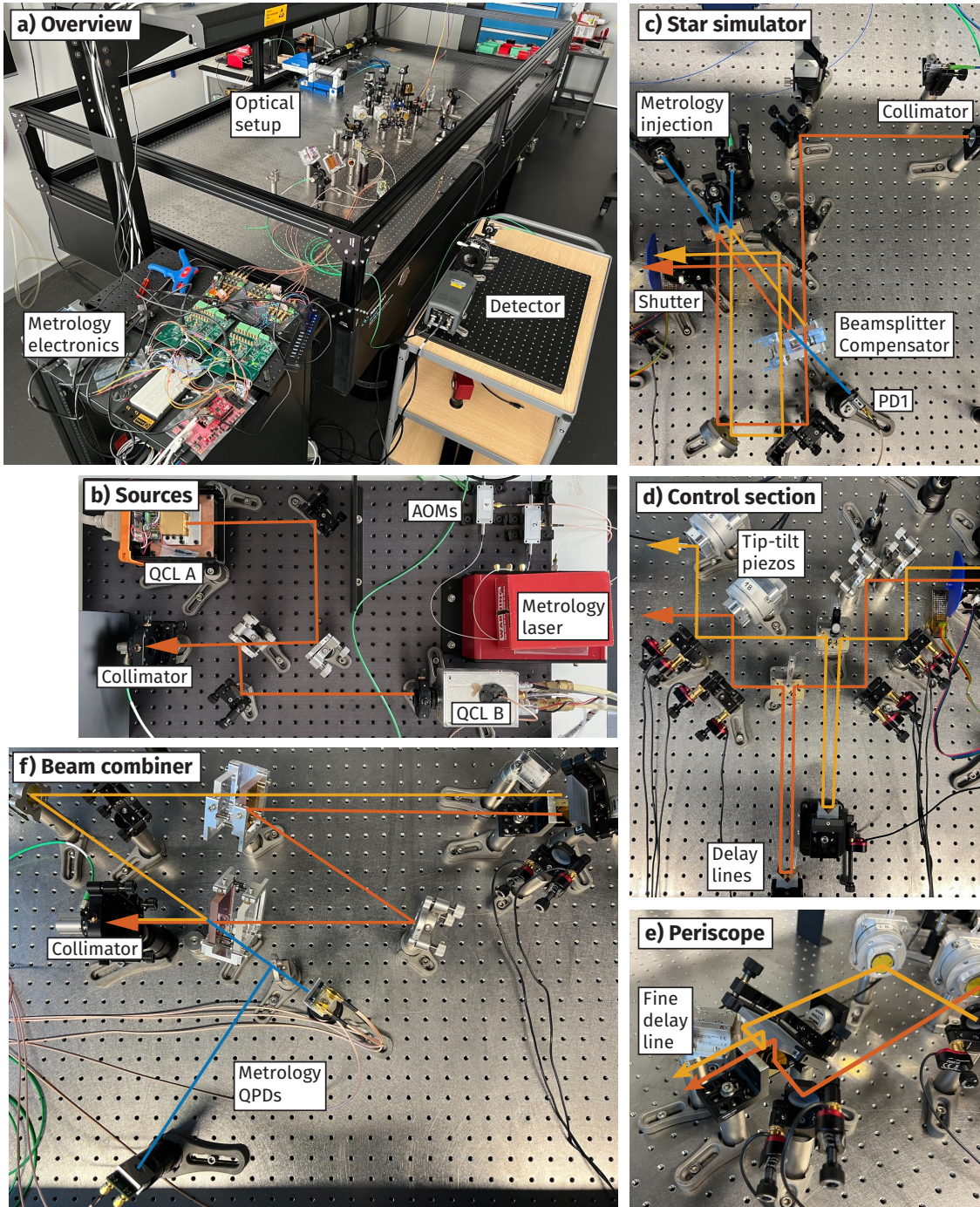


Fig 6: Subsystems of the Warm Bench. a) Overview b) Sources c) Star simulator d) Control section e) Periscope f) Beam combiner.

and therefore accumulates almost identical chromatic and polarization errors. To avoid ghosts and chromatic errors, all beam-splitters that the science beams traverse are wedged and equipped with compensator plates, such that the length of glass seen by each beam is identical. In a future extension, we may require four identical output beams for a Double-Bracewell interferometer, hence requiring a multi-stage system.

3.1.3 *Planet simulator*

To demonstrate that a star is nulled while a planet is still transmitted, we need to simulate a second source. A real planet will have both an off-axis angle, as well as an additional phase-shift compared to the star. As a simpler starting point, part of the stellar light can be split off after the star simulator, tilted slightly, and phase shifted, such that the desired planet signal can be simulated. Because of the large optical path length in the planet simulator, the planet light would be incoherent with the stellar light, as required. However, this does not simulate a realistic planet spectrum, which would be much colder than that of the star. A possible extension is to use a second star simulator with a different blackbody source to produce a more realistic planet. At the output of the planet simulator, we implement a set of beam-shutters that can block either or both beams from entering the setup, which we use for intensity calibration and for background measurements. The planet simulator is currently not implemented on the Warm Bench.

3.1.4 *Correction stage*

The correction stage is the first subsystem in the optical train of NICE that will also be part of the LIFE beam combiner spacecraft, and as such is also the starting point for throughput measurements. We do not model the collector mirrors or the beam transport between collectors and combiner in NICE. The purpose of this section is to control the OPD between the beams and their alignment with respect to the spatial filter at the end of the setup. Two piezo tip/tilt stages per beam allow control of shear and pointing of each beam. A slow delay line with long stroke, based on a slip-stick piezo actuator, is used for the initial OPD scan to find the zero-OPD fringe. A fast piezo delay line stabilizes the OPD during nulling. The fast delay line and the tip/tilt stages are in closed-loop with the metrology system and the fringe tracker.

3.1.5 *Achromatic phase-shifter*

The achromatic phase shifter introduces a relative phase-shift of π between the beams, such that destructive interference is achieved in the beam combiner. It is implemented as a periscope,⁴⁰ which we chose because it is inherently achromatic if well-aligned, as it only uses reflections to achieve the phase shift. Alternative methods, based on transmissive optics such as phase plates, are not feasible for our broad wavelength-range requirement without also requiring further correcting subsystems, such as an adaptive nuller,^{16,41} or splitting the wavelength range into smaller channels.

3.1.6 *Beam combiner and spatial filter*

A modified Mach-Zehnder interferometer⁴² combines the two beams. It offers the advantage of symmetry and thus achromaticity, but it does produce duplicate outputs: two outputs with constructive interference, and two outputs with destructive interference. Only one destructive output is currently available on the Warm Bench, since a second fine delay-line would be required

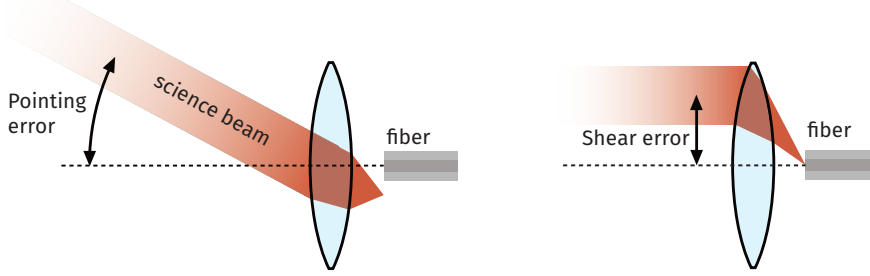


Fig 7: Definition of pointing and shear. Pointing refers to the angular error of the science beam before the collimator, and shear to the lateral displacement of the science beam before the collimator.

to achieve nulls at both outputs simultaneously. Both outputs will be obtained in the future to demonstrate the required system sensitivity.

The beams from the nulled output of the beam combiner, now overlapping and with a π phase difference, are coupled into a single-mode spatial filter. This relaxes the requirements on wavefront-quality, such that the operation of nulling is essentially reduced to matching intensity and phase for each wavelength and polarization mode of the filtered beams. However, since coupling into the fiber depends on the position and angle of the incoming beams, the throughput of the system now strongly depends on alignment, and leakage of higher-order modes will still be present, although highly attenuated. On the Warm Bench, we currently use an off-the-shelf 5 m single-mode InF_3 fiber, and off-axis parabolas as collimators.

3.1.7 Detector

The two outputs from the spatial filter are collimated and spectrally dispersed with a prism. On the Warm Bench, we use an off-the-shelf InSb detector-array at 77 K, located outside of the enclosure to reduce the coupling of vibrations from its cryocooler to the interferometer. In the cryogenic setup, detector options include a HgCdTe array (although such an option may have limited use at the longest wavelengths), or a superconducting detector such as a kinetic inductance detector (KID), which is currently under development for efficient mid-infrared operation.⁴³

3.2 Error budget

The requirement on null depth in NICE from Table 1 can be further broken down into the equal-weight error budget in Table 2. Individual errors in the system contribute according to

$$\langle N \rangle = \frac{1}{4} \left(\langle \delta\phi \rangle^2 + \sigma_{\delta\phi}^2 + \frac{1}{4} \langle \delta\phi_{\text{sp}} \rangle^2 + \langle \delta I \rangle^2 + \sigma_{\delta I}^2 + \frac{1}{4} \langle \delta I_{\text{sp}} \rangle^2 \right), \quad (2)$$

where $\langle N \rangle$ is the mean null depth at a single wavelength and spatial mode, $\delta\phi$ is the phase error between the beams, $\delta I = |I_1 - I_2|/(I_1 + I_2)$ is the intensity mismatch between beams, and terms with an sp-subscript indicate differential errors between the s and p polarization modes. Angled brackets $\langle \dots \rangle$ refer to the mean of a quantity over time, and σ refers to the sample standard deviation over time. More detailed definitions of the terms as well as the derivation of the equation are in Section A. This model assumes an ideal single-mode spatial filter, coherent beams, and that all polarization errors are static in time. The intensity mismatch depends on the coupling efficiency

Table 2: Equal-weight error budget for NICE to achieve the required mean null depth $\langle N \rangle$. For static errors, we put requirements on the mean value of phase $\langle \delta\phi \rangle$ and intensity errors $\langle \delta I \rangle$, while for dynamic errors, we put requirements on their sample standard deviations $\sigma_{\delta\phi}$ and $\sigma_{\delta I}$. The most stringent demands on phase errors are at $4 \mu\text{m}$, and the most stringent demands on intensity errors are at $8 \mu\text{m}$. Polarization errors are assumed static.

Parameter	Wavelength			
	$4 \mu\text{m}$	$8 \mu\text{m}$	$12 \mu\text{m}$	$18 \mu\text{m}$
Required $\langle N \rangle$	$2.0 \cdot 10^{-5}$	$6.8 \cdot 10^{-6}$	$1.8 \cdot 10^{-5}$	$1.0 \cdot 10^{-4}$
<i>Static errors:</i>				
$\langle \delta\phi \rangle$	2.3 nm	2.7 nm	6.7 nm	24 nm
$\langle \delta I \rangle$	0.37 %	0.21 %	0.35 %	0.83 %
$\langle \delta I_{\text{sp}} \rangle$	0.74 %	0.43 %	0.70 %	1.7 %
$\langle \delta\phi_{\text{sp}} \rangle$	4.7 nm	5.4 nm	13 nm	48 nm
<i>Dynamic errors:</i>				
$\sigma_{\delta\phi}$	2.3 nm	2.7 nm	6.7 nm	24 nm
$\sigma_{\delta I}$	0.37 %	0.21 %	0.35 %	0.83 %
σ_{pointing}	16 μrad	25 μrad	47 μrad	110 μrad
σ_{shear}	204 μm	155 μm	199 μm	307 μm
$\sigma_{\text{higher order}}$	0.18 %	0.11 %	0.17 %	0.42 %

of the beams into the single-mode spatial filter, and can be further broken into contributions from pointing error, shear error (see Fig. 7), and higher-order terms such as lab seeing and surface errors. The higher-order contributions are reported as fluctuations in intensity, and can be related to the wavefront error or Strehl ratio.

3.3 Metrology and control system

For NICE to achieve the stability budgeted in Section 3.2, we developed a metrology and control system⁴⁴ to monitor changes in OPD, pointing, and shear, and apply corrections to the fine delay line and the tip/tilt-stages. The metrology system currently implemented on the Warm Bench is not representative of the flight configuration, since we also have to monitor the star simulator and the planet simulator in the testbed, though a similar concept may be used for the LIFE beam combiner internally. The metrology laser is a 100 mW, $1.55 \mu\text{m}$ solid-state laser, used for both OPD and beam position measurements. The OPD metrology is based on a heterodyne interferometer with a phase-meter, while beam positions are measured using the same beams with an intensity-modulation scheme and quadrant photodiodes (QPDs). The metrology beams are overlaid with the science beams in the star simulator, and any error measured in the metrology beams is used as a proxy for errors in the science beams, though drifts and non-common-path errors may occur. One pair of metrology beams propagates backwards and is measured at PD_1 , while the other pair of metrology beams propagates forwards, and is measured at the QPDs at the constructive output of the beam combiner. The system achieves best-case OPD control within 0.7 nm RMS residual metrology error in closed-loop operation with a -3 dB control bandwidth of $\approx 20 \text{ Hz}$, and a measurement bandwidth of 1 kHz. Shear is controlled in closed loop, but at a much slower bandwidth ($\approx 2 \text{ Hz}$), with $\approx 0.2 \mu\text{m}$ RMS residual metrology error with a 100 Hz measurement bandwidth. Pointing is also measured at 100 Hz bandwidth, but pointing control is

not yet implemented. Pointing drifts are slow enough not to contribute significantly to current null measurements.

While the laser metrology can see the full beam path relevant for NICE, LIFE will need a different system to monitor pathlengths between the spacecraft and the star. We foresee a fringe-tracker in the cryogenic NICE setup to demonstrate measuring drifts in OPD at timescales of 0.1 s or longer with realistic flux levels. The OPD control loop will then use fringe tracker measurements at slower frequencies, and metrology measurements for high-frequency control. The fringe tracker will operate in the astronomical K-band ($\approx 2.0 \mu\text{m}$ to $2.4 \mu\text{m}$) from a broadband source, representing the wavelengths of the star below the science band. An integrated photonic device similar to the GRAVITY fringe tracker^{45,46} could be used, and is under development at ETH Zürich.

3.4 Alignment and measurement procedure

The setup is initially aligned by placing the components on the table in approximately the nominal position, and then fine-tuned with an autocollimator and an auxiliary Michelson interferometer to ensure good angular precision. A visible alignment laser that is co-aligned with the science lasers is used for this process. Once fringes are visible at the destructive output of the beam combiner, the spatial filter is placed at their location, and alignment is tuned to maximize coupling into the spatial filter. To find zero OPD, we use the pulsed broadband laser with a coherence length on the order of $100 \mu\text{m}$, and scan the rough delay line until the global minimum of the intensity pattern is reached. At that point, we switch to the narrowband laser, as it is a continuous rather than a pulsed source.

With the beam shutters, we chop between the beams and adjust the tip/tilt mirrors slightly to balance their intensities. We open the beam shutters such that both beams interfere, remove the 0.1 % ND filter in front of the detector, and start the closed-loop control system to stabilize the beams. A short iterative process of optimizing the null depth begins, which consists of manually scanning the OPD setpoint and the shear setpoints until the spot is as dark as possible, and the measurement of the null depth is started. After the null depth measurement, the beam control system is switched off, the ND filter is re-introduced, and a time-series of the intensity of each beam is measured to derive the maximum constructive intensity. For all recordings, an area $\approx 64 \times 64$ pixels on the detector is recorded at $\approx 1000 \text{ kHz}$ sampling rate, with an exposure time of 0.15 ms.

To analyze the data, all recordings are background-subtracted and corrected for the ND filter. The flux in a circular aperture is measured as a function of time. For the intensities I_1 and I_2 , the median of this time series is used as a proxy for the maximum constructive intensity. Note that the beams from the constructive output cannot be used for this, since they do not couple into the same spatial filter, and thus do not experience the time-varying coupling-efficiency into the single-mode fiber as the destructive output. The null depth is finally calculated according to Eq. (1).

4 Results

4.1 Null depth and stability

Figure 8 shows a measurement of a $7.2 \cdot 10^{-6}$ mean null depth over 25 s, using the narrowband $4.7 \mu\text{m}$ laser source, and with a linear polarizer at the output. This meets our requirement of

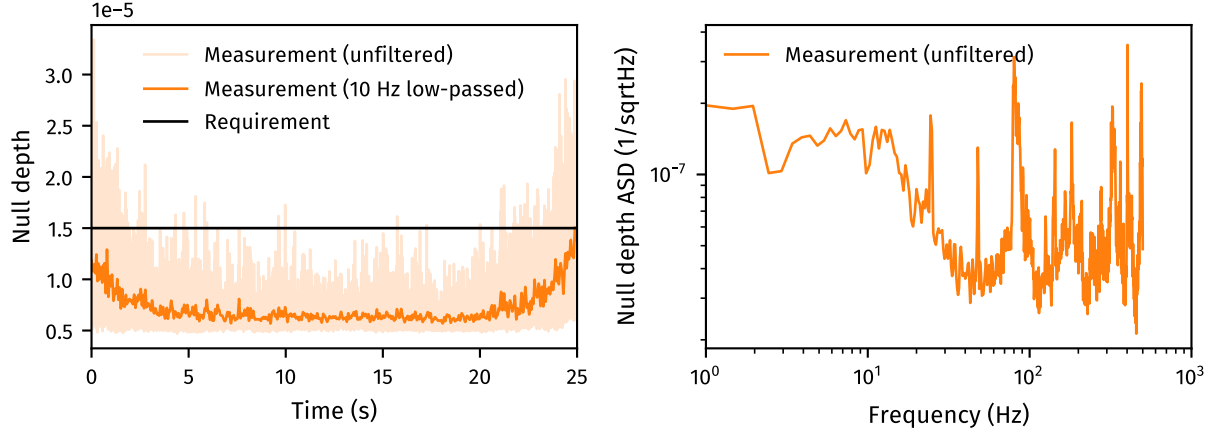


Fig 8: *Left:* The measured null depth meets the requirement for 25 s, before a drift in OPD occurs that was not visible to the metrology system. *Right:* Amplitude spectral density of the same measurement.

Table 3: Throughput measurement of NICE at 4.0 μm with best-effort fiber coupling. Some additional losses occur when balancing intensities between the two science beams. Only one of the two MMZ outputs is currently implemented, and the requirement is thus only half that of the two-output system.

Location	Throughput (%)		
	Measured	Required	Status
Control section	90 ± 2	—	—
Achromatic phase-shifter	95 ± 2	—	—
Beam combiner	40 ± 2	—	—
Spatial filter	63 ± 2	—	—
Total	22 ± 1	17	✓

$1.5 \cdot 10^{-5}$ at 4.7 μm . There is a drift towards the end of the measurement, and the stability of the null is limited to ≈ 25 s. The result was repeatable, with a mean null depth of $< 10^{-5}$ achieved in multiple sessions.

4.2 Throughput

The starting point for the throughput measurement in NICE is at the beginning of the beam control section, since the star simulator and the planet simulator are not part of LIFE. We used the 4.0 μm QCL as a source, and we set the shutter to block one of the science beams at a time, to measure the throughput of each beam independently without interference effects. We used a sensitive mid-IR wavefront sensor to measure the relative power loss of each section, and we used a less sensitive thermal power meter to verify our measurements up to the MMZ, where the power meter was no longer sufficiently sensitive.

Table 3 shows the measured throughput of each section of the setup, as well as the throughput of the full setup. In the numbers presented here, we assume constructive interference for planet light, which is also how the requirement is derived. We measure a throughput of $(22 \pm 1)\%$, which

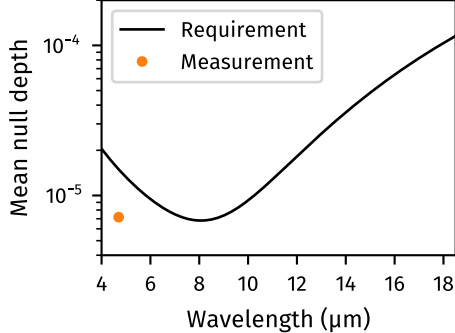


Fig 9: Comparison of measured null depth at $4.7\text{ }\mu\text{m}$ with the required null depth over the mission wavelength range. The measured null depth meets the requirement with a 2x margin, and would almost meet the most stringent requirement at $8\text{ }\mu\text{m}$.

Table 4: The measured residual errors during the null depth measurement meet the error budget for the required null depth. Note that all measurements except for null depth were obtained with the metrology system, so potential offsets or drifts between metrology and science are possible. The pointing measurement was not yet implemented at the time when the nulls were recorded, the values reported here were measured later and are typical for an open enclosure.

Parameter	Measured	Error budget	Status
Mean null depth	$7.17 \cdot 10^{-6}$	$1.5 \cdot 10^{-5}$	✓
$\sigma_{\delta\phi}$	1.2 nm	2.4 nm	✓
σ_{shear}	$0.17\text{ }\mu\text{m}$	$203\text{ }\mu\text{m}$	✓
σ_{pointing}	$\approx 10\text{ }\mu\text{rad}$	$19\text{ }\mu\text{rad}$	~

meets the requirement of 17 % for a single output of the MMZ. With both outputs of the MMZ active, we would require a 34 % throughput.

5 Discussion

5.1 Mean null depth

The measured mean of $7 \cdot 10^{-6}$ null is compliant with the requirement at $4.7\text{ }\mu\text{m}$, and is close to even the deepest requirement of $6.8 \cdot 10^{-6}$ at $8.0\text{ }\mu\text{m}$, as shown in Fig. 9.

A comparison of the measured null depth and errors with the error budget is shown in Table 4. During the measurement, closed-loop OPD control and shear control were active. Shear control was likely not necessary, as even in open-loop, the measured error is far below the error budget. The pointing metrology had not yet been implemented at the time of this measurement, but pointing was later found to be stable within $10\text{ }\mu\text{rad}$ RMS typically, even without an enclosure. Intensity mismatch was not measured during the null, as we do not have access to the single-beam intensities after the spatial filter, and a measurement before the spatial filter would not include the varying coupling efficiency from pointing, shear, or wavefront errors. Measuring the intensities of the beams sequentially after the null measurement was inconclusive because of drifts of the laser intensity during the recordings. Since the measured null meets the requirement, we can however conclude that the intensity mismatch is also compliant with requirements.

5.2 Stability

There is a drift in null depth towards the end of the measurement, which was manually corrected using the delay line (not shown here). The error is thus mostly in the OPD between the science beams, despite the metrology residuals not showing any error of this scale, indicating a drift between science-beam OPD and metrology-beam OPD. We expect this to be a non-common-path error, for example caused by imperfect alignment between metrology and science beams, the different wavelengths between science and metrology, or the science beam traversing a path that is not visible to the metrology, such as the spatial filter.

Regardless of the source of these drifts in the null depth, we anticipate that moving towards cryogenic operation, with a much more stable temperature environment and with minimal lab-seeing, will increase the long-term stability of the system, moving from ≈ 20 s to our requirement of 100 s. Any remaining drifts would then be corrected during an automated recalibration procedure, as described in Section 2.4.

Regarding noise at higher frequencies in the power spectrum in Fig. 8, peaks between 10 Hz to 200 Hz are identified with peaks measured by the OPD metrology, and are likely structural vibrations of the optics. Peaks at higher frequencies are due to intensity instabilities of the laser. They are too small to have a significant impact on mean null depth, but a more stable laser will simplify intensity calibration.

5.3 Spatial filter mode leakage

The most likely source of the drifts in null depth is the spatial filter, as we have seen multiple problems associated with it. First, if the science beams are not well aligned before the spatial filter, we see a leakage of a tip/tilt mode through the spatial filter, where moving the delay line slightly when in a null results in the beam moving vertically on the detector. As a consequence, a null of 10^{-5} or less is then difficult to find, but can be regained after a re-alignment of the setup. This indicates that the spatial filter has insufficient suppression of spatial modes for our purposes. Second, the spatial filter is extremely sensitive to external perturbations. Even slightly touching the fiber while nulling results in a rise of intensity by a factor of ≈ 10 , indicating that some differential error between beams is introduced, possibly from higher-order modes getting stronger, or polarization errors being introduced. Since the metrology beams do not traverse the spatial filters, any errors introduced therein cannot be corrected by the control system.

To alleviate these issues, we are investigating alternative spatial filters, such as hollow core fibers⁴⁷ or photonic crystal fibers,³⁵ that should not introduce parasitic spatial modes. These types of fibers also have the benefit of no Fresnel losses, thus increasing the throughput, functioning at longer wavelengths than the current InF_3 fibers, and are much shorter to reduce the amount of non-common path between the metrology detectors and the science detector, and the sensitivity to environmental perturbations. Alternative solutions, including cladding mode strippers or robust automated injection algorithms, are also being explored.

5.4 Throughput

While there are some caveats to the throughput measurement, which we will explain below, we argue to have demonstrated that the throughput requirement for NICE is achievable from an optical perspective for the shorter wavelength range, and that the remaining challenges for the Warm Bench are mostly on the opto-mechanical side and the alignment strategy.

First, we only have access to one of the two nulled outputs, since we are still developing a method to efficiently couple into two spatial filters simultaneously. For a single output, we meet the requirement for the throughput (22 % measured vs 17 % required), meaning optical interfaces and coatings are efficient enough. Since the optical path of the second output would be nearly identical, the challenge is mostly opto-mechanical.

Second, we currently require a polarizer to hit a deep null, which would effectively halve our throughput if unpolarized light — as would be expected from a planet — was used. We do not expect the throughput to differ for unpolarized light if the polarizer is removed, but achieving the null in both polarization modes simultaneously requires better alignment of the setup and matching of optical surfaces, or alternatively a method to control polarization errors.

Third, the measurement was performed at $4.0\text{ }\mu\text{m}$, representing the lower end of the LIFE science band. The CaF_2 beam-splitters are specified from $2\text{ }\mu\text{m}$ to $8\text{ }\mu\text{m}$, and a broader wavelength range requires different materials or a splitting of the optical path into multiple bands. The splitting ratio of the beam splitters, the reflectivity of the coatings, and the fiber losses will also vary as a function of wavelength; thus more effort is required to develop a broadband instrument.

6 Outlook

With the Warm Bench having demonstrated sufficient throughput and null depth under simplified conditions — a single output, a single polarization mode, and monochromatic light — there are now multiple developments required in parallel to verify the LIFE beam combiner.

6.1 Broadband nulling of unpolarized light on the Warm Bench

The required null has to be achieved with unpolarized light, a broadband source or multiple monochromatic sources, and in both outputs of the beam combiner, while retaining a throughput of more than 34 %. While we expect null depth and spectral bandwidth to be similar to results from previous testbeds, we have more stringent requirements on throughput, and need to build a setup compatible with cryogenic operation. At that point, the Warm Bench will have concluded its primary objective, but will remain in use for prototyping.

6.2 Preparatory cryogenic studies

Transitioning to a cryogenic setup is required to reach the sensitivity for a source of realistic planetary flux-levels. Difficulties include alignment (cooling down may disturb the optical path), materials (matching CTEs, kinematic mounting) and vibrations (cryo-cooler, vacuum pumps), so early experimental verification is essential. We are currently assembling a smaller test-cryostat with an internal volume of $30\text{ cm} \times 20\text{ cm} \times 20\text{ cm}$ to characterize optics at 10 K to 20 K on the level of single components and small assemblies.

6.3 Alignment strategy and compensation mechanisms

Going from moderately broadband light to the full LIFE science band of $4\text{ }\mu\text{m}$ to $18.5\text{ }\mu\text{m}$ will require compensation of chromatic and polarization errors, caused by imperfect alignment or mismatches in coatings. These errors are difficult to predict, so experimental verification is again paramount. There are two approaches to compensating chromatic and polarization errors: active correction with an adaptive nuller, or lower-order independent compensation mechanisms.

The baseline approach is to get close with static alignment before cooling down, and to compensate small residual errors with independent mechanisms, such as moving a compensator plate laterally for first-order control of chromatic errors, rotating the roof prism in the periscope to rotate polarization, and controlling ellipticity errors with a slight intentional misalignment in the tip/tilt stages. While these correction mechanisms are potentially simple to implement, they pose strict requirements on all optical tolerances, as they can only compensate for small low-order errors.

Alternatively, the Adaptive Nuller⁴¹ is a potential risk mitigator against a wide range of optical errors, as it gives full control over phase and amplitude as a function of wavelength and polarization mode. It is expected to loosen tolerances on coatings and alignment by orders of magnitude, and has the option to simplify and even make redundant many components in the optical path, such as removing the need for a second nulled output in the beam combiner. Such a device has been successfully demonstrated with high contrast¹⁶ from $8\text{ }\mu\text{m}$ to $12\text{ }\mu\text{m}$, but not at the high sensitivity and cryogenic temperatures required for NICE, and questions remain as to the stroke and fidelity needed of the requisite deformable mirror.

6.4 Spatial filtering and injection optics

An efficient spatial filter is necessary to loosen requirements on wavefront quality. While these devices exist off-the-shelf separately as narrowband mid-infrared devices and broadband visible-light devices,⁴⁸ an efficient spatial filter that works broadband in the mid-infrared has not yet been experimentally demonstrated. Tightly coupled with the spatial filter itself are the injection optics, which in the case of LIFE have to efficiently couple a top-hat beam into a waveguide with a nearly Gaussian fundamental mode. Techniques such as phase-induced amplitude apodization (PIAA),^{49,50} which can reshape the beam into a near-Gaussian profile, are promising not only to increase coupling, but also extend the broadband response via a wavelength dependent beam diameter. Both technologies are currently under investigation.³⁵

6.5 Photonic integrated devices

Photonic integrated devices, essentially an optical setup on a microchip, may offer great potential for miniaturization, increased stability, and repeatable modular manufacturing. They are commonly used in modern ground-based nullers (NOTT,^{51,52} GLINT^{24,25}) for these reasons, but they are almost entirely unexplored beyond $4\text{ }\mu\text{m}$ because of a lack of transparent substrates and mature processes, with recent developments pushing towards the longer end of LIFE's bandpass.⁵³

6.6 Missing subsystems

Currently, we only simulate an on-axis star, which we aim to extinguish through nulling. A realistic demonstration of the instrument should measure the throughput of an off-axis planet while nulling the star, which requires a planet simulator. Furthermore, LIFE cannot rely on internal metrology systems to measure the path from the star to the collector mirrors, so a fringe tracker has to be demonstrated, using a source at $\approx 2\text{ }\mu\text{m}$. Finally, LIFE is a Double-Bracewell nuller, while NICE is currently a Single-Bracewell design. A copy of the setup and a final cross-combiner stage are needed to verify the full four-beam architecture.

7 Conclusion

We are building the Nulling Interferometry Cryogenic Experiment (NICE), a technology demonstrator and development testbed for the beam combiner of the LIFE space mission. While the requirements for NICE are not yet fully derived from the LIFE science case and the LIFE reference design in a systematic manner, we argue that the requirements we have set for NICE are likely more ambitious than necessary to ensure compliance in the future. NICE requires a $\approx 10^{-5}$ null depth from 4 μm to 18.5 μm while maintaining a high throughput of 34 % in a cryogenic environment. At ambient conditions, using a narrowband 4.7 μm source and a polarizer at the output, we have achieved a mean raw null depth of $7 \cdot 10^{-6}$ over 25 s, deeper than any previously published result in the M-band, as well as a throughput of 22 % from one of the two nulled outputs of the beam combiner. Both null depth and throughput are compliant with requirements. We expect the Warm Bench to be a polarization-agnostic and more broadband nullder in the near future.

While the principle of the measurement has thus been demonstrated in a simplified environment, and the strategy for a sensitive cryogenic instrument has been laid out, we also emphasize some technological gaps that lie ahead of us. Some of the subsystems required for NICE, such as the spatial filter and the compensation mechanisms required for nulling over two octaves of spectral bandpass, while conceptually defined, are still experimentally unverified. Further studies are required before NICE can transition to a cryogenic setup.

Appendix

Use of AI tools

Github Copilot was used as an auto-complete tool while writing the code for data analysis and numerical evaluation of the error budget. No other AI tools were used in the preparation of this work.

Disclosures

The authors declare that there are no financial interests, commercial affiliations, or other potential conflicts of interest that could have influenced the objectivity of this research or the writing of this paper.

Code, Data, and Materials Availability

The data presented in this article, as well as the source code to analyze the data and produce the tables and figures in this article, are publicly available on Github at <https://github.com/thomabir/NICE-Paper-I>.

Acknowledgements

Part of this work has been carried out within the framework of the National Centre of Competence in Research PlanetS supported by the Swiss National Science Foundation under grants 51NF40_182901 and 51NF40_205606. NICE is financially supported by the Swiss Prodex program directed by the Swiss Space Office. This project is supported by Rudolf Bär via the ETH Zurich Foundation.

Appendix A: Derivation of the error budget

Here, we derive how the mean null depth during an observation can be broken down into individual error terms. The goal is not to tolerance the optical setup in detail, but to derive the higher-level error terms that can later be used for optical tolerancing. Much of the derivation follows the work of Serabyn,⁵⁴ with some modifications, such as not assuming a lossless 50/50 beam-splitter, and also breaking down the intensity mismatch into pointing and shear errors. We present the derivation here mostly for the sake of consistency and easy reference.

A.1 Null depth for a single polarization mode

For a single wavelength, polarization mode, and spatial mode, the only quantities that affect the null depth are the intensities I_1 , I_2 , and the phases ϕ_1 , ϕ_2 of the two beams. The electric field amplitudes at the detector for two arbitrary beams are then

$$E_1 = \sqrt{I_1} \exp(i\phi_1), \quad E_2 = \sqrt{I_2} \exp(i\phi_2).$$

We define the maximum constructive intensity $I_+ = I_1 + I_2 + 2\sqrt{I_1 I_2}$, the phase error $\delta\phi = |\phi_1 - \phi_2|$, and the intensity mismatch $\delta I = |I_1 - I_2|/(I_1 + I_2)$. The instantaneous nulled intensity at the destructive output is then $I_- = |E_1 - E_2|^2$, and the null depth is

$$N = \frac{I_-}{I_+} = \frac{1 - \sqrt{1 - \delta I^2} \cos(\delta\phi)}{1 + \sqrt{1 - \delta I^2}} \approx \frac{1}{4}(\delta\phi^2 + \delta I^2),$$

where the final expression is the second-order Taylor approximation for δI , $\delta\phi$ around zero.

A.2 Null depth for both polarization modes

Consider the case of two orthogonal polarization modes, such as s and p , still for a single wavelength and spatial mode,

$$N_s \approx \frac{1}{4}(\delta\phi_s^2 + \delta I_s^2), \quad N_p \approx \frac{1}{4}(\delta\phi_p^2 + \delta I_p^2),$$

where both modes may have independent errors in phase and intensity. The null depth when both modes are combined on the same detector is the mean of the two null depths,

$$N = \frac{N_s + N_p}{2} = \frac{1}{4} \left(\delta\phi^2 + \frac{1}{4} \delta\phi_{sp}^2 + \delta I^2 + \frac{1}{4} \delta I_{sp}^2 \right), \quad (3)$$

where

$$\begin{aligned} \delta\phi &= \frac{\delta\phi_s + \delta\phi_p}{2}, & \text{Average phase error in } s \text{ and } p \text{ mode,} \\ \delta\phi_{sp} &= |\delta\phi_s - \delta\phi_p|, & \text{Difference in phase mismatch between } s \text{ and } p \text{ mode,} \\ \delta I &= \frac{\delta I_s + \delta I_p}{2}, & \text{Average intensity mismatch in } s \text{ and } p \text{ mode,} \\ \delta I_{sp} &= |\delta I_s - \delta I_p|, & \text{Difference in intensity mismatch between } s \text{ and } p \text{ mode.} \end{aligned}$$

A.3 Dynamic top-level error budget

In a real instrument, errors will vary over time. To produce a first-order estimate of the resulting mean null depth, we assume that all errors are independent white Gaussian noise over time, and that errors are small, so the lowest non-zero terms in the Taylor series are used. We further assume that all polarization errors are static in time. This results in

$$\langle N \rangle(\lambda) = \frac{1}{4} \left(\langle \delta\phi \rangle^2 + \sigma_{\delta\phi}^2 + \frac{1}{4} \langle \delta\phi_{\text{sp}} \rangle^2 + \langle \delta I \rangle^2 + \sigma_{\delta I}^2 + \frac{1}{4} \langle \delta I_{\text{sp}} \rangle^2 \right), \quad (4)$$

where angled brackets $\langle \dots \rangle$ denote the mean over time, and σ denotes the sample standard deviation over time. This equation is used to derive the equal-weight top-level error budget in Table 2.

A.4 Influence of pointing and shear errors

Any change in the shear and pointing of the science beams leads to a change in coupling efficiency into the spatial filter, which will affect the null depth. To derive the impact of these errors, we first derive how a static shear or pointing offset affects throughput and null depth, and then derive the dynamic effect. We assume Gaussian beams and waveguides with Gaussian modes.

We use the Fresnel approximation to analytically model the action of focusing with a lens. The field E_1 at the focal plane of the lens is then related to the field E_0 just before the lens by [55, p. 103]

$$E_1(x, y) = -\frac{i}{f\lambda} \exp \left[\frac{i\pi}{f\lambda} (x^2 + y^2) \right] \iint_{\mathbb{R}^2} E_0(x', y') \exp \left[-\frac{2\pi i}{f\lambda} (xx' + yy') \right] dx' dy', \quad (5)$$

where λ is the wavelength, and f the focal length of the lens.

Coupling into a single mode fiber is modeled by the overlap integral of the electric field E_1 at the entrance of the fiber with the Gaussian mode ψ of the fiber. The fiber is characterized by its mode field radius w_f , which is the waist radius of the Gaussian beam that propagates in the fiber. The normalized fiber mode is then

$$\psi(x, y) = \sqrt{\frac{2}{\pi w_f^2}} \exp \left(-\frac{x^2 + y^2}{w_f^2} \right),$$

where *normalized* means that $\iint_{\mathbb{R}^2} \psi(x, y)^2 dx dy = 1$. Before defining the coupling efficiency, we introduce the overlap integral

$$\langle E_1 | \psi \rangle = \iint_{\mathbb{R}^2} E_1(x, y) \psi^*(x, y) dx dy,$$

where ψ^* denotes the complex conjugate of ψ . The coupling efficiency η is then defined as the power ratio of input beam and the output beam of the fiber, [56, p. 21.8]

$$\eta = \frac{|\langle E_1 | \psi \rangle|^2}{\langle E_1 | E_1^* \rangle \langle \psi | \psi^* \rangle}. \quad (6)$$

We neglect here effects such as Fresnel reflection at the fiber facet and propagation losses, since we are only interested in how a change in pointing or shear changes the throughput, not in

absolute throughput.

A Gaussian beam propagating along the z -axis has at its waist, i.e. its narrowest point, an electric field

$$E(x, y) = E_0 \exp \left(-\frac{x^2 + y^2}{w_0^2} \right), \quad (7)$$

where $x^2 + y^2 = r^2$ is the squared distance from the optical axis, E_0 is the electric field at the origin, and w_0 is the waist radius, which is the radius where the amplitude falls off to $1/e$.

A Gaussian beam that is tilted by a small angle α along the x -axis is obtained by adding a linear phase shift $ikx\alpha$ to Eq. (7),

$$E_0(x, y) = E_0 \exp \left(-\frac{x^2 + y^2}{w_0^2} + ikx\alpha \right). \quad (8)$$

We set $E_0 = 1$ from now, since the amplitude would anyway cancel out in the throughput calculation. To find how a tilted Gaussian beam propagates to the focal plane, we plug Eq. (8) for E_0 into Eq. (5) and evaluate the integral, which yields

$$E_1(x, y) = -\frac{i\pi w_0^2}{f\lambda} \exp \left(-\frac{1}{4}\alpha^2 k^2 + \frac{\pi\alpha k w_0^2 x}{f\lambda} - \frac{\pi^2 w_0^2 (x^2 + y^2)}{f^2 \lambda^2} \right), \quad (9)$$

where a term $i\pi r^2/(f\lambda)$ in the exponent was dropped as it is small compared to the other terms. To calculate the coupling efficiency, we plug Eq. (9) into the Eq. (6), and evaluate:

$$\eta_{\text{pointing}} = \exp \left(-\frac{\pi^2 \alpha^2 w_0^2}{\lambda^2} \right) = 1 - \frac{\pi^2 \alpha^2 w_0^2}{\lambda^2} + \mathcal{O}(\alpha^4). \quad (10)$$

We used here that $f = \pi w_0 w_f / \lambda$ is the focal length required to focus the initial beam with waist w_0 onto the fiber profile with waist w_f , which leads to all occurrences of w_f canceling out.

If the beam has a lateral offset o with respect to the optical axis along the x -direction, then the initial beam profile is

$$E_0(x, y) = E_0 \exp \left[-\frac{(o - x)^2 + y^2}{w_0^2} \right].$$

We follow the same procedure as for the tilted beam to arrive at the throughput

$$\eta_{\text{shear}} = \exp \left(-\frac{o^2}{w_0^2} \right) = 1 - \frac{o^2}{w_0^2} + \mathcal{O}(o^4). \quad (11)$$

The corresponding intensity mismatch that would result from an error of this kind, assuming a single beam is affected, is

$$\delta I = \frac{1 - \eta}{1 + \eta} = \tanh \left(\frac{\chi^2}{2} \right) = \frac{\chi^2}{2} + \mathcal{O}(\chi^4), \quad (12)$$

where the functional form $\eta = \exp(-\chi^2)$ is assumed. This yields

$$\delta I_{\text{shear}} \approx \frac{o^2}{2w_0^2}, \quad \delta I_{\text{pointing}} \approx \frac{\alpha^2 \pi^2 w_0^2}{2\lambda^2}. \quad (13)$$

To translate from static errors into dynamic errors, we use higher-order Gaussian error propagation:

$$\sigma_{\delta I}^2 = \sigma_\chi^2 \left(\frac{d\delta I}{d\chi} \right)^2 + \frac{1}{2} \sigma_\chi^4 \left(\frac{d^2 \delta I}{d\chi^2} \right)^4 + \mathcal{O}(\sigma_\chi^6) \approx \frac{\sigma_\chi^4}{2}, \quad (14)$$

where we used that the mean of χ is zero (no DC error). For a combined error in shear and pointing, we plug in for χ to find

$$\sigma_{\delta I}^2 = \frac{1}{2} \left(\frac{\sigma_o}{w_0} \right)^4 + \frac{1}{2} \left(\frac{\sigma_\alpha w_0 \pi}{\lambda} \right)^4, \quad (15)$$

which is used to derive the contribution of shear and pointing to the error budget in Table 2.

References

- 1 S. P. Quanz, M. Ottiger, E. Fontanet, *et al.*, “Large interferometer for exoplanets (life): I. improved exoplanet detection yield estimates for a large mid-infrared space-interferometer mission,” *Astronomy & Astrophysics* **664**, A21 (2022).
- 2 B. S. Konrad, E. Alei, S. P. Quanz, *et al.*, “Large interferometer for exoplanets (life): Iii. spectral resolution, wavelength range, and sensitivity requirements based on atmospheric retrieval analyses of an exo-earth,” *Astronomy & Astrophysics* **664**, A23 (2022).
- 3 R. N. Bracewell, “Detecting nonsolar planets by spinning infrared interferometer,” *Nature* **274** (1978).
- 4 A. M. Glauser, S. P. Quanz, J. Hansen, *et al.*, “The large interferometer for exoplanets (life): a space mission for mid-infrared nulling interferometry,” in *Optical and Infrared Interferometry and Imaging IX*, S. Sallum, J. Sanchez-Bermudez, and J. Kammerer, Eds., 48, SPIE (2024).
- 5 J. R. P. Angel and N. J. Woolf, “An imaging nulling interferometer to study extrasolar planets,” *The Astrophysical Journal* **475**, 373–379 (1997).
- 6 F. A. Dannert, M. Ottiger, S. P. Quanz, *et al.*, “Large interferometer for exoplanets (life): II. signal simulation, signal extraction, and fundamental exoplanet parameters from single-epoch observations,” *Astronomy & Astrophysics* **664**, A22 (2022).
- 7 L. Kaltenegger and M. Fridlund, “The darwin mission: Search for extra-solar planets,” *Advances in Space Research* **36**(6), 1114–1122 (2005).
- 8 C. Cockell, A. Léger, M. Fridlund, *et al.*, “Darwin—a mission to detect and search for life on extrasolar planets,” *Astrobiology* **9**, 1–22 (2009).
- 9 C. A. Beichman, N. J. Woolf, and C. A. Lindensmith, *The Terrestrial Planet Finder (TPF) : a NASA Origins Program to search for habitable planets* (1999).
- 10 S. Martin, “The flight instrument design for the terrestrial planet finder interferometer,” in *Techniques and Instrumentation for Detection of Exoplanets II*, D. R. Coulter, Ed., **5905**, 590503, SPIE (2005).

- 11 P. Gabor, P. A. Schuller, B. Chazelas, *et al.*, “Tests of achromatic phase shifters performed on the synapse test bench: a progress report,” in *Optical and Infrared Interferometry*, **7013**, 70134O, SPIE (2008).
- 12 V. Weber, M. Barillot, P. Haguenauer, *et al.*, “Nulling interferometer based on an integrated optics combiner,” in *New Frontiers in Stellar Interferometry*, W. A. Traub, Ed., **5491**, 842, SPIE (2004).
- 13 C. Buisset, X. Rejeaunier, Y. Rabbia, *et al.*, “Multi-axial nulling interferometry: demonstration of deep nulling and investigations of polarization effects,” in *Advances in Stellar Interferometry*, J. D. Monnier and W. C. Danchi, Eds., **6268**, 626819, SPIE (2006).
- 14 J.-M. Le Duigou, J. Lozi, F. Cassaing, *et al.*, “Final results of the persee experiment,” in *International Conference on Space Optics – ICSO 2012*, E. Armandillo, N. Karafolas, and B. Cugny, Eds., 124, SPIE (2017).
- 15 S. Martin, A. Booth, K. Liewer, *et al.*, “High performance testbed for four-beam infrared interferometric nulling and exoplanet detection,” *Applied Optics* **51**, 3907 (2012).
- 16 R. D. Peters, O. P. Lay, and M. Jeganathan, “Broadband phase and intensity compensation with a deformable mirror for an interferometric nuller,” *Applied Optics* **47**, 3920 (2008).
- 17 R. O. Gappinger, R. T. Diaz, A. Ksendzov, *et al.*, “Experimental evaluation of achromatic phase shifters for mid-infrared starlight suppression,” *Applied Optics* **48**, 868 (2009).
- 18 P. M. Hinz, J. R. P. Angel, W. F. Hoffmann, *et al.*, “First results of nulling interferometry with the Multiple-Mirror Telescope,” in *Astronomical Interferometry*, R. D. Reasenberg, Ed., **3350**, 439 – 447, International Society for Optics and Photonics, SPIE (1998).
- 19 B. Mennesson, S. Crawford, E. Serabyn, *et al.*, “Laboratory performance of the keck interferometer nulling beam combiner,” in *Earths: DARWIN/TPF and the Search for Extrasolar Terrestrial Planets*, M. Fridlund, T. Henning, and H. Lacoste, Eds., *ESA Special Publication* **539**, 525–528 (2003).
- 20 E. Serabyn, A. Booth, M. M. Colavita, *et al.*, “Science observations with the keck interferometer nuller,” in *Advances in Stellar Interferometry*, J. D. Monnier and W. C. Danchi, Eds., **6268**, 626815, SPIE (2006).
- 21 B. Mennesson, C. Hanot, E. Serabyn, *et al.*, “High-contrast stellar observations within the diffraction limit at the palomar hale telescope,” *The Astrophysical Journal* **743**, 178 (2011).
- 22 D. Defrère, P. M. Hinz, A. J. Skemer, *et al.*, “First-light lbt nulling interferometric observations: Warm exozodiacal dust resolved within a few au of eta crv,” *The Astrophysical Journal* **799**, 42 (2015).
- 23 D. Defrère, P. M. Hinz, B. Mennesson, *et al.*, “Nulling data reduction and on-sky performance of the large binocular telescope interferometer,” *The Astrophysical Journal* **824**, 66 (2016).
- 24 B. R. M. Norris, N. Cvetojevic, T. Lagadec, *et al.*, “First on-sky demonstration of an integrated-photonic nulling interferometer: the glint instrument,” *Monthly Notices of the Royal Astronomical Society* **491**, 4180–4193 (2019).
- 25 M.-A. Martinod, B. Norris, P. Tuthill, *et al.*, “Scalable photonic-based nulling interferometry with the dispersed multi-baseline glint instrument,” *Nature Communications* **12** (2021).
- 26 E. A. Spalding, E. Arcadi, G. Douglas, *et al.*, “The glint nulling interferometer: improving nulls for high-contrast imaging,” in *Optical and Infrared Interferometry and Imaging IX*, S. Sal-lum, J. Sanchez-Bermudez, and J. Kammerer, Eds., 6, SPIE (2024).

27 D. Defr  re, O. Absil, J.-P. Berger, *et al.*, “The path towards high-contrast imaging with the vlti: the hi-5 project,” *Experimental Astronomy* **46**, 475–495 (2018).

28 D. Defr  re, A. Bigioli, C. Dandumont, *et al.*, “L-band nulling interferometry at the vlti with asgard/hi-5: status and plans,” in *Optical and Infrared Interferometry and Imaging VIII*, A. M  rand, S. Sallum, and J. Sanchez-Bermudez, Eds., SPIE (2022).

29 R. Laugier, D. Defr  re, J. Woillez, *et al.*, “Asgard/nott: L-band nulling interferometry at the vlti: I. simulating the expected high-contrast performance,” *Astronomy & Astrophysics* **671**, A110 (2023).

30 M. Ranganathan, T. Birbacher, J. T. Hansen, *et al.*, “The nulling interferometer cryogenic experiment: the warm phase,” in *Optical and Infrared Interferometry and Imaging IX*, S. Sallum, J. Sanchez-Bermudez, and J. Kammerer, Eds., 52, SPIE (2024).

31 E. Douglas, N. Zimmerman, G. Ruane, *et al.*, “Review of high-contrast imaging systems for current and future ground- and space-based telescopes i: coronagraph design methods and optical performance metrics,” in *Space Telescopes and Instrumentation 2018: Optical, Infrared, and Millimeter Wave*, H. A. MacEwen, M. Lystrup, G. G. Fazio, *et al.*, Eds., 98, SPIE (2018).

32 F. A. Dannert, *How Quiet Is LIFE? Performance of Nulling Interferometers under Instrumental and Fundamental Noise*. PhD thesis, ETH Zurich, Zurich (2025).

33 J. T. Hansen and M. J. Ireland, “Large interferometer for exoplanets (life): Iv. ideal kernel-nulling array architectures for a space-based mid-infrared nulling interferometer,” *Astronomy & Astrophysics* **664**, A52 (2022).

34 O. P. Lay, “Systematic errors in nulling interferometers,” *Applied Optics* **43**, 6100–6123 (2004).

35 M. J. Ireland, S. Madden, and L. Rapp, “Spatial filtering for the large interferometer for exoplanets (life) mission,” in *Optical and Infrared Interferometry and Imaging IX*, S. Sallum, J. Sanchez-Bermudez, and J. Kammerer, Eds., 49, SPIE (2024).

36 F. A. Dannert, P. A. Huber, T. Birbacher, *et al.*, “Consequences of non-gaussian instrumental noise in perturbed nulling interferometers,” *The Astronomical Journal* **170**, 193 (2025).

37 J. Lozi, F. Cassaing, J. M. Le Duigou, *et al.*, “Persee: experimental results on the cophased nulling bench,” in *Optical and Infrared Interferometry II*, 7734, 77342M, SPIE (2010).

38 P. Gabor, B. Chazelas, F. Brachet, *et al.*, “Stabilising a nulling interferometer using optical path difference dithering,” *Astronomy & Astrophysics* **483**, 365–369 (2008).

39 J. T. Hansen, M. J. Ireland, and R. Laugier, “Large interferometer for exoplanets (life): Vii. practical implementation of a five-telescope kernel-nulling beam combiner with a discussion on instrumental uncertainties and redundancy benefits,” *Astronomy & Astrophysics* **670**, A57 (2023).

40 Y. Rabbia, J. Gay, J.-P. Rivet, *et al.*, “Achromatic Phase Shifters: The “Mirror” Approaches,” in *GENIE - DARWIN Workshop - Hunting for Planets*, H. Lacoste, Ed., *ESA Special Publication* **522**, 14.1 (2003).

41 O. P. Lay, M. Jeganathan, and R. Peters, “Adaptive nulling: a new enabling technology for interferometric exo-planet detection,” in *Techniques and Instrumentation for Detection of Exoplanets*, D. R. Coulter, Ed., **5170**, 103, SPIE (2003).

42 E. Serabyn and M. M. Colavita, “Fully symmetric nulling beam combiners,” *Applied Optics* **40**, 1668 (2001).

43 W. G. Ras, K. Kouwenhoven, D. J. Thoen, *et al.*, “Experimental demonstration of photon counting with kinetic inductance detectors at mid-infrared wavelengths,” in *X-Ray, Optical, and Infrared Detectors for Astronomy XI*, PC1310305, SPIE (2024).

44 T. Birbacher, A. M. Glauser, M. Ranganathan, *et al.*, “Beam metrology and control for the nulling interferometry cryogenic experiment,” in *Optical and Infrared Interferometry and Imaging IX*, S. Sallum, J. Sanchez-Bermudez, and J. Kammerer, Eds., 115, SPIE (2024).

45 K. Perraut, L. Jocou, J. P. Berger, *et al.*, “Single-mode waveguides for gravity: I. the cryogenic 4-telescope integrated optics beam combiner,” *Astronomy & Astrophysics* **614**, A70 (2018).

46 S. Lacour, R. Dembet, R. Abuter, *et al.*, “The gravity fringe tracker,” *Astronomy & Astrophysics* **624**, A99 (2019).

47 J. M. Kriesel, N. Gat, B. E. Bernacki, *et al.*, “Hollow core fiber optics for mid-wave and long-wave infrared spectroscopy,” in *Chemical, Biological, Radiological, Nuclear, and Explosives (CBRNE) Sensing XII*, **8018**, 80180V, SPIE (2011).

48 T. A. Birks, J. C. Knight, and P. S. J. Russell, “Endlessly single-mode photonic crystal fiber,” *Optics Letters* **22**, 961 (1997).

49 O. Guyon, “Phase-induced amplitude apodization of telescope pupils for extrasolar terrestrial planet imaging,” *Astronomy & Astrophysics* **404**, 379–387 (2003).

50 N. Jovanovic, C. Schwab, O. Guyon, *et al.*, “Efficient injection from large telescopes into single-mode fibres: Enabling the era of ultra-precision astronomy,” *Astronomy & Astrophysics* **604**, A122 (2017).

51 G. Garreau, A. Bigioli, R. Laugier, *et al.*, “Asgard/nott: first lab assembly and experimental results,” in *Optical and Infrared Interferometry and Imaging IX*, S. Sallum, J. Sanchez-Bermudez, and J. Kammerer, Eds., 25, SPIE (2024).

52 A. Sanny, L. Labadie, S. Gross, *et al.*, “Asgard/nott: L -band nulling interferometry at the vlti: Iii. the mid-infrared integrated optics beam combiner for nott,” *Astronomy & Astrophysics* **705**, A37 (2026).

53 M. Montesinos-Ballester, A. M. Glauser, L. Miller, *et al.*, “Low loss optical integrated waveguides operating in a broad mid-infrared range,” in *Advances in Optical and Mechanical Technologies for Telescopes and Instrumentation VI*, R. Navarro and R. Jedamzik, Eds., 252, SPIE (2024).

54 E. Serabyn, “Nulling interferometry: symmetry requirements and experimental results,” in *Interferometry in Optical Astronomy*, P. J. Lena and A. Quirrenbach, Eds., SPIE (2000).

55 J. W. Goodman, *Introduction to Fourier Optics*, McGraw-Hill, 2 ed. (1996).

56 M. Bass, Ed., *Handbook of Optics, Volume 1*, McGraw-Hill, 3 ed. (2010).

List of Figures

- 1 History of best measured nulls
- 2 Comparison of an ideal nullder with a perturbed nullder
- 3 Requirement on the null depth power spectrum.
- 4 Preliminary optical diagram of NICE
- 5 Optical diagram of the Warm Bench

- 6 Pictures of the Warm Bench
- 7 Definition of pointing and shear
- 8 Measured null depth
- 9 Null depth over wavelength

List of Tables

- 1 Requirements
- 2 Error budget
- 3 Throughput measurement
- 4 Null depth residual error analysis